Electromagnetic Science
vol. x, no. x, , March xxxx
https://doi.org/10.23919/emsci.2024.0051

Research Article

Achieving Many-Fold Reduction in Active Elements with a Highly-Directive Beam-Steerable Huygens Box Antenna

Kayode Adedotun Oyesina[1] and Alex M. H. Wong[1,2]

1. *Department of Electrical Engineering*, *City University of Hong Kong*, *Hong Kong SAR*, *China*
2. *State Key Laboratory of Terahertz and Millimeter Waves*, *City University of Hong Kong*, *Hong Kong SAR*, *China*

Corresponding author: Alex M. H. Wong, Email: Alex.mh.wong@cityu.edu.hk.

Abstract — Recent explorations and advancements in communications systems have sparked a renewed fascination with beam-steerable high-gain antennas. While conventional active phased arrays have been long seen as a feasible solution, the associated cost is a major impediment for electrically large millimeter-wave apertures. In this paper, we present an all-metal metamaterial-loaded Huygens box antenna that facilitates independent steering of radiation in azimuth and elevation directions and a dramatic reduction in the number of phased elements. The antenna encloses an artificial dielectric medium with an active Huygens metasurface arranged around the enclosure's periphery. We present simulation and experiment results for a representative $4\lambda_0 \times 4\lambda_0$ square aperture. The results show that the antenna radiates similarly to a phased array of similar aperture size, with a quadratic-to-linear reduction ratio in the number of required elements, leading to over 10-fold reduction for large-aperture antennas. The tremendous reduction in the number of excited elements positions the antenna as a cost-saving alternative, especially in large aperture mm-wave regime.

Keywords — Huygens sources, metasurface, phased arrays, beam steering, directive antennas.
Citation — Kayode Adedotun Oyesina and Alex M. H. Wong, "Achieving many-fold reduction in active elements with a highly-directive beam-steerable huygens box antenna," *Electromagnetic Science*, vol. x, no. x, article no. , xxxx. doi: 10.23919/emsci.2024.0051.

I. Introduction

Directive and beam-steerable antennas play a vital role in modern communication systems by improving signal quality, extending range, and reducing interference through precise signal directionality [1]–[3]. The steering mechanism of such antennas can be broadly categorized into mechanical and electronic beam steering. Mechanical steering involves the physical movement of some parts of the antenna system [4], [5]. For such antennas, the steering speed and mechanical failure of moving parts are major causes of concern. On the other hand, electronic beam steering uses electronic circuitry to implement required amplitude and phase modulations that facilitate beam steering without physically moving the antennas [6]–[8]. Therefore, the electronically steered phased array stands out as a widely accepted solution for achieving directive beam-steering as it meets the demands of applications requiring continuous and real-time radiation steering, offering desirable attributes such as lightweight design, versatility, rapid response, and seamless integration with other electronic components and integrated circuits. A limiting factor, however, is the required phase-shifting circuitry. Since elements are arranged over the aperture at separations around $\lambda/2$, the required number of antennas (and hence the cost) rises sharply with the required gain and the operating frequency. Moreover, these additions can also lead to a significant increase in the volume and weight of the antenna system [7].

Various solutions have been explored to simplify the feed network for phased array systems. Irregular phased array architectures like clustered, thinned, and sparse arrays have been explored. While subarray configurations are used to reduce feed network complexity in the clustered array [9], [10], the thinned and sparse arrays achieve antenna simplicity by selectively exciting a subset of elements of the array or by omitting some elements from the array [8], [11]–[13]. These irregular arrays achieve high-gain beamforming with reduced radiating or phasing elements at the expense of reduced directivity, worsened sidelobe levels

Electromagnetic Science

and/or reduced tunability as the number of control points becomes limited, since the antennas either have wider average spacing or are excited in subgroups. Furthermore, reconfigurable lenses have been demonstrated to achieve highly directive beam steering [14], [15]. These lenses refocus power from a radiating element to achieve beam steering through a dynamic adjustment of the lens focal length using reconfigurable elements. However, the number of reconfigurable elements also scales with the aperture area. Also, switched beam antennas [16]–[18] that do not require amplitude and phase modulation of antenna elements have been reported. In most cases, a few input ports are aligned along the focal plane of a lens, with each input port corresponding to a particular beam-pointing direction. However, these static realisations do not allow for continuous beam steering, and sometimes, a full overlap of the 3-dB beamwidth of the generated beams cannot be achieved, leading to blind spots.

Recently, the introduction of engineered electromagnetic metamaterials and metasurfaces has significantly improved antenna technology. Engineered electromagnetic materials are materials specially made to exhibit unconventional electromagnetic properties [19]. For instance, materials and surfaces have been built to reflect or diffract electromagnetic waves to anomalous directions, control the absorption, focus the EM wave, control the polarization and shape the wavefront [19]–[21]. Furthermore, due to the ability of such engineered materials to overcome many of the constraints imposed by properties of naturally occurring materials, they have found interesting applications in enhancing many aspects of antenna performance such as size reduction [21], [22], directivity and bandwidth enhancement [23]–[25], and antenna decoupling [26]–[29], among other applications.

In recent developments, the Huygens source has been leveraged for a new phase array architecture that has led to a significant reduction in the number of elements than achievable with previous techniques. The Huygens box [30]–[32] is a metallic cavity inside which arbitrary electromagnetic waves can be synthesized. A directive radiation can be achieved through perforations on the Huygens box top surface. Three models of such antennas have been introduced. The peripherally excited array (PEX) proposed in [33], [34] excites perforations on the cavity's top surface with an underlying slow cavity wave. Due to the usage of a dense dielectric, the realisable reduction ratio is limited to an elemental separation of $\lambda/2$ where $\lambda = \lambda_0/\sqrt{\varepsilon_r}$. The necessary momentum contribution from the top plate, hence, limits the beam-pointing directions. On the other hand, the Transverse Magnetic Mode 1 Huygens box antenna (TM1 HBA) in [35] excites a propagating wave in an air-filled cavity. While this allows for an element separation larger than that in the PEX, the TM1 cavity wave was synthesized using two layers of the Huygens elements, raising the number of required elements by a factor of two, thereby raising the antenna's vertical profile. The Transverse Electromagnetic Huygens box antenna (TEM HBA) in [35]–[38] excites a superluminal wave in a sub-unity refractive index cavity. This allows for an even larger spacing between elements than half free-space wavelength. In addition, the TEM HBA achieves independent control of the azimuth and elevation radiations.

In this paper, we present an experimental demonstration of the highly directive and steerable TEM Huygens box antenna that achieves a dramatic reduction in the number of required elements when compared to a phased array. The all-metal antenna comprises a square radiation aperture enclosed by a metallic cavity, the periphery of which is aligned with the active Huygens sources arranged at appropriate separation. The cavity is filled with an enabling metamaterial region formed by a 2D array of metallic rods. By properly exciting the Huygens sources, travelling plane waves of controllable amplitude, phase and propagation direction can be generated, allowing one to steer the direction of multiple cavity waves with great freedom. We translate this freedom into beam steering capability by adding sub-wavelength perforations on the top metallic plate to allow the cavity wave to leak into free space. The beam can be arbitrarily steered in the azimuthal and elevation directions; multi-beam and radiation pattern engineering can also be facilitated by superimposing plane waves. Crucially, since the number of elements now depends on the aperture ***perimeter*** rather than the aperture ***area***, the number of excitation elements can be reduced many-fold (for example, a 10-fold reduction for a $20\lambda_0 \times 20\lambda_0$ antenna) while maintaining the same directivity. This reduction ratio leads to large savings in component cost with increased aperture size, making it attractive in large aperture mm-wave applications.

In the following “Theory” section, we will elucidate the radiation mechanism and the enabling sub-unity refractive index medium. The “Results” section presents the simulation results and a proof-of-concept experimental demonstration. In the “Discussions” section, we examine the HBA's sensitivity and discuss the TEM HBA in relation to the phased array. Finally, we conclude in the “Conclusion” section.

II. Theory

1. Antenna formulation and radiation mechanism

The Huygens source is a forward radiating source usually composed of co-located and orthogonal electric and magnetic dipoles. Many structures of the Huygens source have been reported in literature. These Huygens sources have been applied as antennas on their own [39], [40], used to form surfaces for unconventional wave manipulations [20], [41], or for antenna enhancement [20], [21], among other applications. A simplified active Huygens source was proposed in [42] and used to synthesize propagating electromagnetic waves in a metallic confinement called the Huygens box [32]. We provide a brief overview in the following. Our Huygens box is formed by arranging the simplified active Huygens sources along the perimeter of a region of interest, with the active elements implementing a boundary of electric and magnetic surface currents that controls electromagnetic waves on both sides of the boundary. Figure 1(a) shows a model of a $m\lambda_0 \times m\lambda_0 \times h$ Huygens box. The dotted red line indicates an equivalent-principle-based boundary of magnetic and electric currents that supports EM fields inside and outside the boundary. Here, the cavity field lies inside the region, while the field outside the boundary is zero. The cavity wave $\{\boldsymbol{E}_{\text{cav}}, \boldsymbol{H}_{\text{cav}}\}$ is related to the surface currents, $\{\boldsymbol{J}_s, \boldsymbol{M}_s\}$,through the equivalence principle by

$$\begin{aligned} \boldsymbol{J}_s &= -\widehat{\boldsymbol{n}} \times \boldsymbol{H}_{\text{cav}} \\ \boldsymbol{M}_s &= \widehat{\boldsymbol{n}} \times \boldsymbol{E}_{\text{cav}} \end{aligned} \tag{1}$$

where $\widehat{\boldsymbol{n}}$ is an outward pointing normal. Applying (1) everywhere along the boundary of the Huygens box, one can find the required surface currents necessary on the boundary to synthesize any arbitrary cavity wave comprising a superposition of TEz plane waves

$$\begin{aligned} \boldsymbol{E}_{\text{cav}} &= \sum_{i=1}^{N} \left\{ \mathrm{E}_{i0} e^{-j(k_{ix}x + k_{iy}y)} \hat{\boldsymbol{z}} \right\} \\ \boldsymbol{H}_{\text{cav}} &= \sum_{i=1}^{N} \left\{ \frac{\mathrm{E}_{i0}}{\eta} e^{-j(k_{ix}x + k_{iy}y)} (\sin\varphi_i \hat{\boldsymbol{x}} - \cos\varphi_i \hat{\boldsymbol{y}}) \right\} \end{aligned} \tag{2}$$

in a Huygens box of refractive index n where $\eta = 120\pi/n$, $k = 2\pi n/\lambda_0$, $k_{ix} = k\cos\varphi_i$ and $k_{iy} = k\sin\varphi_i$ where φ_i, the i'th plane wave's propagation direction inside the cavity, is referenced to the x-axis. With $\{\boldsymbol{J}_s, \boldsymbol{M}_s\}$ known, the excitation current needed for the constituent Huygens sources to produce $\{J_s, M_s\}$are then calculated using

$$\mathrm{I} = j\frac{sM_s}{k\eta w} \tag{3}$$

where s is the separation between Huygens sources and w is as defined in Figure 1(a). Here, $M_s = \boldsymbol{M}_s \cdot (\hat{\boldsymbol{n}} \times \hat{\boldsymbol{z}})$, where $(\cdot)$ and $(\times)$ denote the inner and cross products respectively.

In this paper, we formulate a highly directive antenna by coupling a propagating plane wave in a Huygens box to free space radiation through perforations on the Huygens box's top surface. We consider a square aperture of dimension $4\lambda_0 \times 4\lambda_0$, where λ_0 is the free-space wavelength. We arrange the Huygens sources at $\lambda_0/2$ separation from one another to form a boundary separating an enclosed region from the outer free space. Figure 1(a) shows the TEM HBA, with subwavelength perforations in a rectangular lattice on the top surface and the Huygens sources on the Huygens box boundary. The elements are arranged on the xy-plane at locations (x_i, y_i) where $i = 1, 2, 3 \ldots N$. We impress the necessary excitation currents calculated using (3) to synthesize a propagating TEz plane wave in the Huygens box and couple the synthesized cavity wave to directive ra-

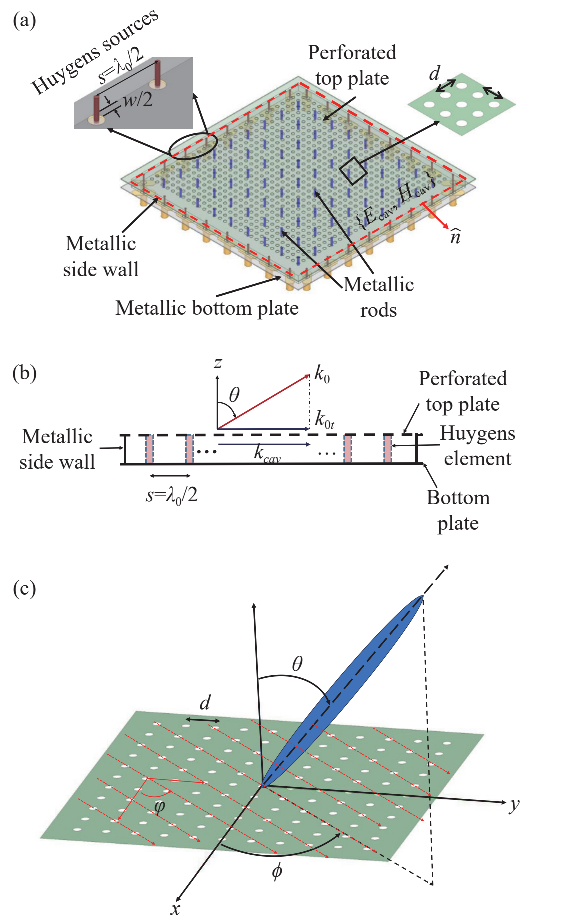

Figure 1 The TEM Huygens box antenna. (a) Antenna model (b) A side view of the antenna depicting its radiation mechanism (c) Pencil beam generation from a 2D array of slots excited by an underlying propagating wave.

diation through a phase-matching operation. Figure 1(b) shows a side view of the Huygens box antenna and depicts its radiation mechanism. We couple the synthesized plane wave, in a direction of $(\varphi, 90°)$ ($\theta = 90°$ denotes propagation on the xy-plane), to directive radiation at $(\phi,\ \theta)$ by matching the propagating cavity wave's wavenumber, k_{cav} to the radiated wave's horizontal spatial frequency, k_{0t}, where

$$k_{cav} = k_0 n \tag{4}$$

and

$$k_{0t} = k_0 \sin\theta. \tag{5}$$

Combining both relations in (4) and (5), we have

$$n = \sin\theta \tag{6}$$

where n is the refractive index of the Huygens box and θ is the radiated beam's elevation direction measured from broadside.

From (6), we observe that the enclosed region needs to have a refractive index less than unity as we seek to radiate a wave at an angular range of $-90^\circ \le \theta \le 90^\circ$. We achieve this sub-unity refractive index using the rodded dielectric medium which we will introduce in the next section.

2. The sub-unity refractive index medium

Here, we briefly review the construction of artificial dielectrics with unconventional refractive indices which we subsequently employ to achieve sub-unity refractive index in our Huygens box antenna. It is known that by arranging conducting obstacles in a periodic manner, with such obstacles separated at distances not more than half wavelength, media with indices less than unity could be formed. Some explored obstacles include spheres, circular discs, rods and planar strips [43], [44]. For simplicity and practicality, we have adopted the rodded dielectric medium as depicted in Figure 2(a). Metallic rods of radius r are arranged in the x-y plane in free space, with inter-element separations of a and b along the x and y directions respectively. $\boldsymbol{E}$, $\boldsymbol{H}$ and $\hat{\boldsymbol{k}}$ are the electric field, magnetic field and wave propagation direction respectively. The E-field is polarized along z – the direction of the rods. A medium so formed can be modelled as shunt inductances across a transmission line with free space impedance Z_0 and propagation constant γ_0 as shown in Figure 2(b). An analysis of this model results in the dispersion relationship relating the index of the medium to the spacing by [44]

$$\cos\frac{2\pi bn}{\lambda_0} = \cos\frac{2\pi b}{\lambda_0} + \frac{\lambda_0 \sin(2\pi b/\lambda_0)}{2a\ln(a/2\pi r)} \tag{7}$$

provided that $a \ll \lambda_0$ and $r \ll a$, where n is the refractive index, r is the radius of the metallic rods, λ_0 is the free space wavelength and a and b are the rod separations in x and y directions respectively. We consider the specialized case of equal separation, b, in both x- and y-directions, in which case

$$\cos\frac{2\pi bn}{\lambda_0} = \cos\frac{2\pi b}{\lambda_0} + \frac{\lambda_0 \sin(2\pi b/\lambda_0)}{2b\ln(b/2\pi r)}. \tag{8}$$

After rearrangement, we express the refractive index as

$$n = \frac{\lambda_0}{2\pi b}\cos^{-1}\left[\cos\frac{2\pi b}{\lambda_0} + \frac{\lambda_0 \sin(2\pi b/\lambda_0)}{2b\ln(b/2\pi r)}\right]. \tag{9}$$

As an example, we have calculated and plotted the refractive index against rod spacing using copper rods of radius $r = 0.25$ mm for operation at 30GHz according to (9) in Figure 2(c) (solid black curve). The index peaks at $n = 1$ when $b = \lambda_0/2$. Furthermore, we simulate the structure shown in Figure 2(a) in HFSS, treating the system as a conventional two-port network from which the S-parameters can be easily extracted. Refs. [45], [46] have related the reflection and transmission coefficients and the effective constitutive parameters of such metamaterials. This relationship is summarized in (10) and (11)

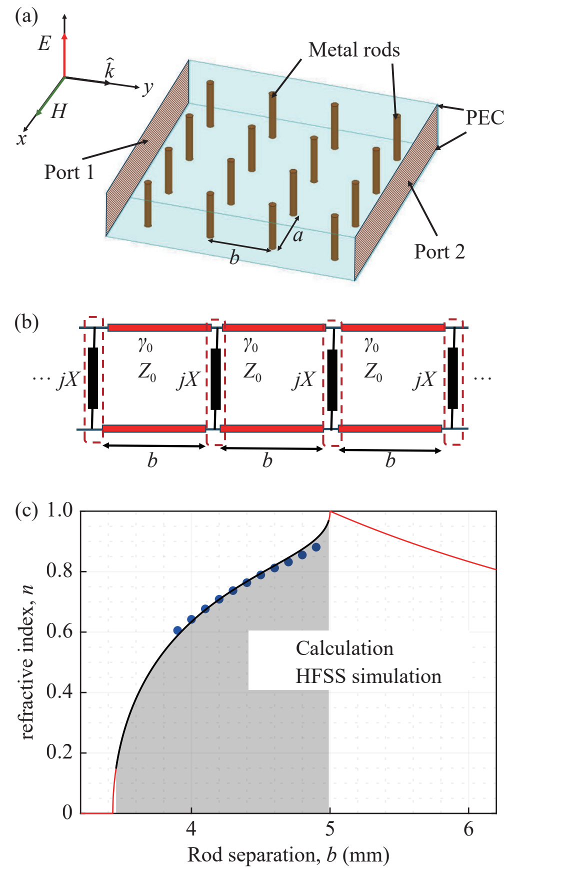

Figure 2 The sub-unity refractive index artificial dielectric medium formulation. (a) Typical rodded medium that can realize sub-unity refractive index. The E-field is polarized along the direction of the rods. ε_r, μ_r and n can be extracted using the two-port S-parameters. (b) The rodded artificial dielectric medium equivalent circuit. The field in the vicinity of the conductive rods are modeled as shunt reactances across a transmission line. (c) A plot of the calculated and extracted refractive index as a function of rods spacing, b, at 30 GHz. The shaded region depicts a region of purely real refractive index at spacings less than $\lambda_0/2$.

$$e^{jnk_0 d} = \frac{S_{21}}{1 - S_{11}\left(\frac{z'-1}{z'+1}\right)} \tag{10}$$

$$n = \frac{1}{k_0 d}\left(\left[\left(\Im\left(\ln e^{jnk_0 d}\right) + 2p\pi\right)\right] - j\Re\left[\ln e^{jnk_0 d}\right]\right) \tag{11}$$

where S_{11} and S_{21} are reflection and transmission parameters respectively, d is the distance from the input port to the output port location, k_0 denotes the free space wavenumber and p denotes the branch of the logarithm function of (10). z' (dimensionless) is the impedance of the fundamental mode, normalized to the free space intrinsic impedance. Using (10) and (11), we extract the rodded medium's refractive indices at different rod separations. The extracted refractive indices are marked by the red dots in Figure 2(c). The simulated values agree well with the calculated ones.

3. The TEM huygens box antenna versus the peripherally excited array (PEX)

At this point, it is necessary to distinguish the TEM HBA's radiation mechanism from that of the PEX proposed in [30], [31]. The PEX is similar in structure to the HBA and has also achieved a many-fold reduction in the number of elements. The operation of the two antenna architectures can be explained using a typical perforated aperture excited by an underlying cavity wave propagating at an angle, ϕ, as depicted in Figure 1(c). The underlying cavity wave produces a radiated pencil beam towards azimuth and elevation directions φ and θ, respectively. The perforations on the top surface of the antennas are excited by a synthesized cavity wave with wavevector $k = k_0 n(\cos\varphi, \sin\varphi, 0)$, where $n < 1$ in the TEM HBA case and $n > 1$ in the PEX case. Applying the phase matching operation between the propagating cavity wave and free space to predict the antenna radiation yields [47]

$$k_0 n\cos\varphi d + 2\pi a_m = k_0 d\sin\theta\cos\phi \tag{12}$$

$$k_0 n\sin\varphi d + 2\pi a_n = k_0 d\sin\theta\sin\phi \tag{13}$$

where (a_m, a_n) are integers representing the different Floquet modes that can radiate in air. These phase-matching equations are based on the assumption of an infinitely periodic 2D array of unit cells capable of supporting the excitation of Floquet modes and remain valid when applied to relatively large finite apertures. After some mathematical manipulations, one can find that a set of beams can emanate from the perforated aperture which have elevation (θ) and azimuth (ϕ) directions given by

$$\sin^2\theta = n^2 + \frac{4\pi^2}{k_0^2 d^2}\left(a_m^2 + a_n^2\right) + \frac{4\pi n}{k_0 d}\left[a_m\cos\varphi + a_n\sin\varphi\right] \tag{14}$$

$$\tan\phi = \frac{n\sin\varphi + 2\pi a_m / k_0 d}{n\cos\varphi + 2\pi a_n / k_0 d}. \tag{15}$$

The key difference between the TEM HBA and the PEX is that while the perforations for the TEM HBA are excited by a superluminal cavity wave in a sub-unity index medium, the perforations for the PEX are excited by a subluminal cavity wave in a dense dielectric medium. The usage of a sub-unity refractive index medium in the TEM HBA allows for a more aggressive discretization of the peripheral boundary than the PEX, as inter-element spacing must be limited to $s < \lambda/2$ with $\lambda = \lambda_0/n$, in order to avoid the generation of spurious cavity waves. Furthermore, it is clear from (14) that the PEX cannot radiate to the fundamental (0,0) mode as there exists no valid solution for (14) when $a_m = a_n = 0$. On the other hand, the TEM HBA has a sub-unity refractive index cavity, and hence has valid solution for the radiated beam-pointing direction when $a_m = a_n = 0$. Under this condition, (14) reduces to (6), thus the elevation radiation direction is solely determined by the cavity's refractive index, regardless of the azimuthal radiation direction. Furthermore, (15) shows that $\phi = \varphi$ when $a_m = a_n = 0$, hence the azimuthal radiation direction (ϕ) corresponds to the cavity wave's travel direction (φ). Since the elevation (θ) and azimuth (ϕ) directions of the radiated pencil beams for any travel direction (φ) are not coupled, one may freely steer the beam in the azimuthal direction without affecting the elevation direction. Furthermore, since no momentum contribution is required from the top plate, any subwavelength perforation pattern will suffice, avoiding complex considerations regarding the shape, size, or pattern of the perforation, and the corresponding azimuthal variations arising from the perforation pattern. A summary of the key differences is provided in Table 1. Therefore, the TEM HBA holds significant advantages over the PEX in that it uses fewer elements, has a simpler design for perforations, and can achieve independent steering in both azimuth and elevation directions.

Table 1 A summary of key differences between the TEM HBA and the PEX.

	Ref. [33], [34]	This work
Cavity	Dense dielectric	Sub-unity index metamaterial
Cavity wave	Slow wave	Fast wave
Element spacing	$< \lambda_0/2$	$> \lambda_0/2$
Radiation mechanism	Involves momentum contribution from top plate	Does not involve momentum contribution from top plate
Azimuth and elevation direction control	Coupled	Allows for independent control
Broadside radiation	Supported	Not supported

III. Results

In this Section, we present our results. We used the commercial full-wave simulator Ansys HFSS to perform simulations for the HBA. A model of the TEM HBA is shown in Figure 1(a). The cavity walls of the Huygens box are modelled as aluminum plates. We construct the peripheral Huygens elements as the metal-backed single filament active Huygens source of [32], [42] with filament-to- cavity-wall separation $w/2 = \lambda_0/20$ and waveguide height $h = \lambda_0/5$. The latter is chosen so that only the fundamental TEM mode is synthesized, which remains invariant along the z-direction within the cavity. The top plate is perforated with circular holes of diameter 2 mm and pitch 2.4 mm. These perforations are sub-wavelength and thus do not contribute momentum to the radiated wave. Also, we model the metamaterial region as a 2D array of metallic rods as discussed in Section II-2. In all simulations presented, we employ a center-to-center element spacing of $\lambda_0/2$ unless otherwise stated. As we posit this device for millimeter wave operation where component cost for phase-shifting circuitry becomes significant, we have chosen the operating frequency to be 30 GHz. However, the Huygens box antenna is easily scalable to different frequency regimes.

1. Single beam radiation and beam steering

We show here the generation of directive antenna patterns emanating from a single propagating plane wave within the

Huygens box. First, we generate a propagating plane wave in the Huygens box of Figure 1(a). In this case, the excitation currents all have equal amplitude. To couple the generated cavity wave to directive radiation at (ϕ,θ), we fill the enclosure with a metamaterial region formed by arranging equispaced conductive rods of radius 0.25 mm at 4.2 mm apart. As investigated in the formulation described in Section II-2, this rodded medium exhibits a refractive index of 0.7092 at the operation frequency, which facilitates radiation at an elevation angle of $\theta = 45^\circ$.

With the elevation direction set to $\theta = 45^\circ$, we control the azimuth (ϕ) direction by varying the cavity wave's travel direction. Figure 3(a) - (h) shows the radiated pencil beam at some sample azimuth angles. We show that complete 360° steering is achieved. We show in Figure 3(i)-(j) the 2D radiation patterns along the $\theta = 45^\circ$ and respective ϕ plane cuts. The beam is clearly steered in the azimuth direction without affecting its elevation direction.

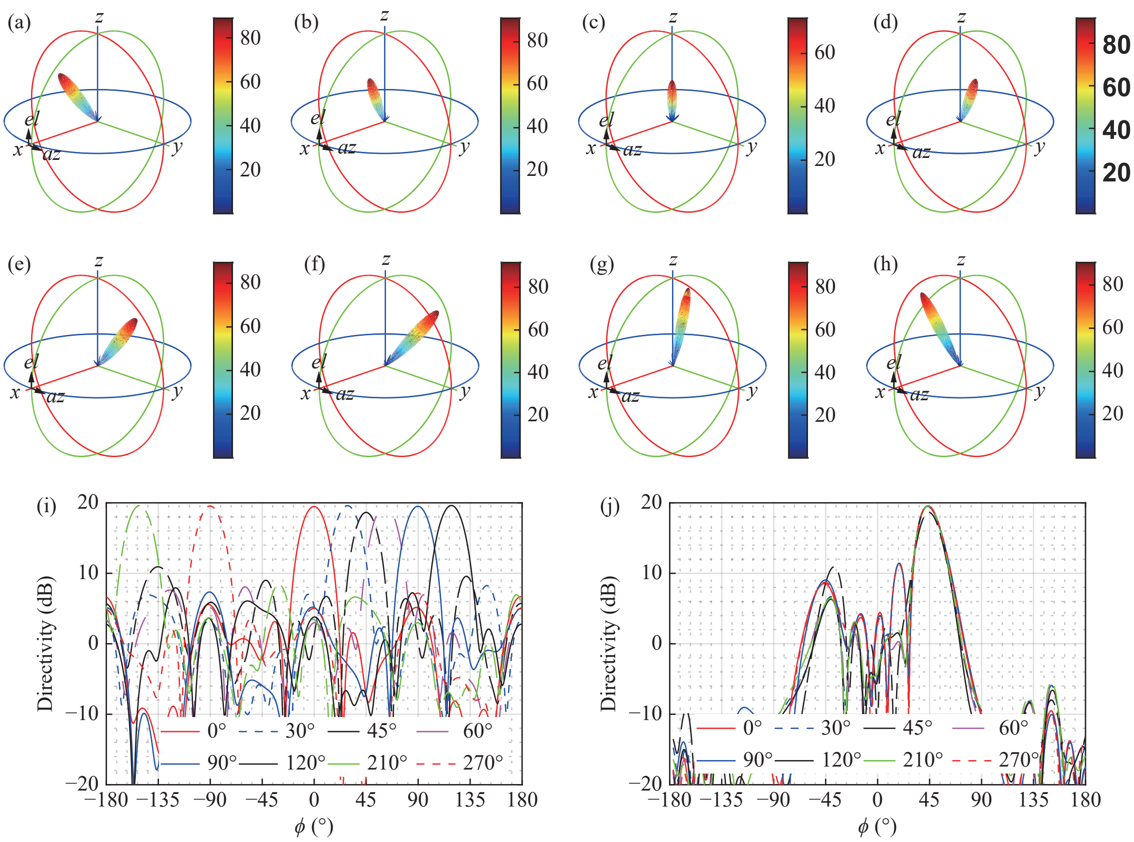

Figure 3 Single beam radiation from single propagating plane wave and azimuthal beam steering. 3D polar patterns are shown for azimuth angles (a) $\phi = 0^\circ$, (b) $\phi = 30^\circ$, (c) $\phi = 45^\circ$, (d) $\phi = 60^\circ$, (e) $\phi = 90^\circ$, (f) $\phi = 120^\circ$, (g) $\phi = 180^\circ$, (h) $\phi = 210^\circ$, and (i) $\phi = 270^\circ$. Beam steering demonstration, with (i) showing 2D pattern at $\theta = 45^\circ$ plane and (j) 2D pattern at respective ϕ planes.

Table 2 summarizes the azimuth beam steering results for single pencil beam generation. The table presents the directivities as well as the 3 dB beamwidths for different azimuth angles ϕ. We show results for selected azimuth angles within $0^\circ \le \phi < 90^\circ$ as beam characteristics for larger azimuth angles can be inferred by symmetry: for example, the beam characteristics at 120°, 210° and 300° are the same as those for $\phi = 30^\circ$. Directivities of around 20 dB are achieved, which is comparable to a phased array of a similar aperture size according to $D = \frac{4\pi}{\lambda^2} A_e$ where $A_e = \cos\theta$ is the effective aperture area. The 3 dB beamwidth averaging about 18° also conforms to the expected value for a phased array of the same aperture size. Small deviations in directivity and beamwidth may have resulted from simulation convergence effects: imperfect simulation convergence may have caused a slight deviation of the refractive index depending on the propagation direction ϕ. Also, slight reflections off the cavity walls affect the purity of the generated wave mode and contribute to the slight reduction in directivity observed.

Next, we demonstrate beam steering in the elevation direction by varying the separation, b, between the metallic rods that form the sub-unity refractive index metamaterial region (the relationship between refractive index and rod spacing is given by (9) and detailed in Section II-2). We calculate the corresponding refractive indices for three rod separations $b = 3.90$ mm, 4.20 mm and 4.75 mm. Thereafter, we implement and simulate the rodded medium in HFSS and extract the refractive index value using the s-parameters. Table 3 shows the calculated and the extracted refractive indices for the selected rod separations. The refractive indices, and subsequently the elevation angles, extract-

Table 2 Summary of results for the 30 GHz $4\lambda_0 \times 4\lambda_0$ TEM HBA single beam radiation.

$\phi(°)$	$\varphi(°)$	$\theta(°)$	Directivity (dB)	3 dB Beamwidth	
				φ-plane (°)	θ-plane (°)
0	0	45	19.5	18.6	21.2
30	30	45	19.6	18.3	21
45	45	45	18.6	18.8	19.7
60	60	45	19.6	18.4	21
90	90	45	19.5	18.3	21.2
120	120	45	19.6	18.1	20.9
270	270	45	19.9	18.6	21.3

ed from the simulation agree with the values calculated using the effective medium theory. We show in Figure 4 the resulting antenna patterns when we couple a plane wave propagating at $\phi = 0°$ in the Huygens box to directive radiation at the aforementioned rod separations. We observe that the beam is steered to corresponding elevation angles $\theta = 37°$, $45°$, and $57°$ while the azimuth angle is retained at $\varphi = 0°$ in all cases. Our device achieves full 360° steerability in the azimuthal direction. However, since our device is subjected to (6), broadside radiation is not possible, as n will have to be zero. Also, similar to other phased arrays, the projected aperture becomes small at near-grazing angles for a $4\lambda_0 \times 4\lambda_0$ aperture, limiting the directivity of the antenna for $\varphi > 60°$. One can radiate to large oblique angles ($60° < \theta < 90°$) by increasing the size of the Huygens' box.

Table 3 Elevation steering for the 30 GHz $4\lambda_0 \times 4\lambda_0$ TEM HBA using the artificial dielectric medium's rod separation.

b(mm)	Calculation		Simulation	
	n	$\theta(°)$	n	$\theta(°)$
3.9	0.5886	36.1	0.6059	37.3
4.2	0.708	45.2	0.7092	45.2
4.75	0.8462	59.3	0.8352	57.2

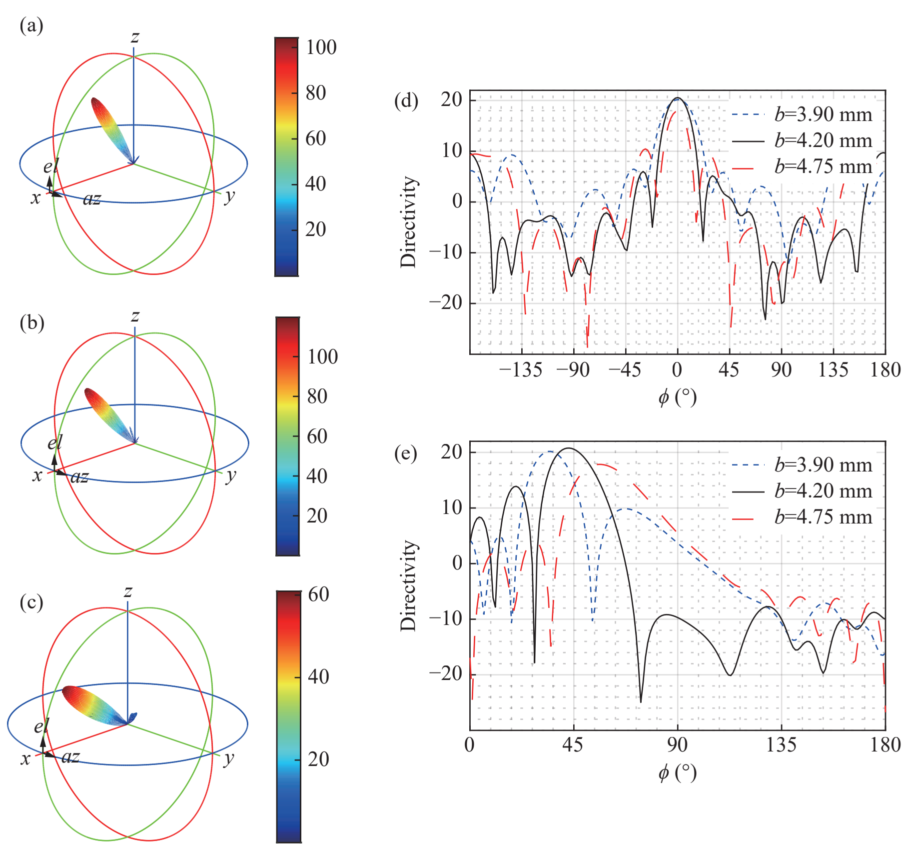

Figure 4 Elevation steering using cavity's refractive index. (a) – (c) show 3D polar radiation patterns at $(\phi,\theta) = (0°,34°)$, $(0°,45°)$ and $(0°,57°)$ respectively for $b = 3.9$ mm, 4.2 mm and 4.75 mm . (d) 2D planar cut of the radiation patterns at respective ϕ planes. (e) 2D planar cut of the radiation patterns at respective θ planes.

2. Multiple beam radiation

The Huygens box allows for the synthesis of arbitrary waveforms. We now explore the synthesis of multiple plane waves and radiation emanating from such. The excitation of multiple plane waves in the Huygens box is achievable by vectorially adding all constituent plane waves excitations. We define a superposition of plane waves in arbitrary directions specified by φ_i by (2), where N is the number of plane waves, E_{i0} and ϕ_i represent the amplitude and phase of the i'th plane wave, η is the intrinsic impedance within the rodded medium, and $k_{ix} = k_0 n\cos\varphi_i$ and $k_{iy} = k_0 n\sin\varphi_i$ are the x-and y-components of respective wave vectors for each constituent plane wave. $\boldsymbol{E}_{\rm cav}$ and $\boldsymbol{H}_{\rm cav}$ are then applied to calculate the excitation currents using (3).

We consider the case of two plane waves radiating at arbitrary azimuth angles. Figure 5(a) - (c) show the pencil beam pairs radiated from the Huygens box for three pairs of directions: $(\phi_1,\phi_2) = (40°, 270°)$ $(40°, 310°)$ and $(45°, 135°)$. The elevation angle for all beams is 45°. Figure 5(d) - (f) show the 2D planar cut along the $\theta = 45°$ plane while Figure 5(g) - (i) plot the radiation pattern along the respective ϕ planes. In these cases, the pair of beams exhibit roughly equal amplitudes. Table 4 summarizes the results for the three beam pairs presented. Generally, the directivities for the main lobes are observed to be around 16 dB. These values are 3 dB lower than the directivities in the single beam cases, implying a roughly equal split of power into each beam direction. We note that since the multiple plane waves that are eventually coupled to multibeam radiation travel in different directions, there is no coupling between the multiple beams.

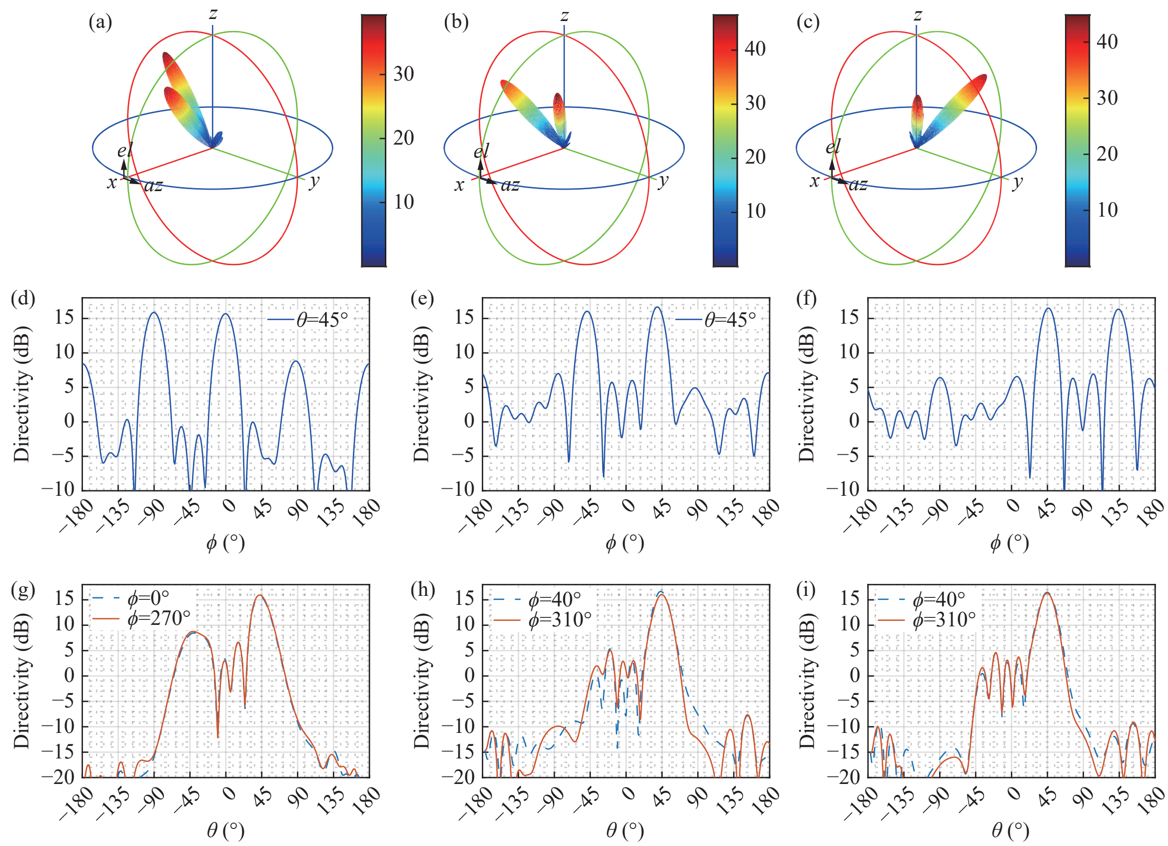

Figure 5 Dual beam radiation. (a) - (c) show 3D radiation pattern for beam pair (a) $(\phi,\theta) = (0°, 45°)$ and $(270°, 45°)$, (b) $(\phi,\theta) = (40°, 45°)$ and $(310°, 45°)$, and (c) $(\phi,\theta) = (45°, 45°)$ and $(135°, 45°)$ with the dual beams having equal intensities. (d) - (f) 2D planar cut of (a) - (c) at $\theta = 45°$-plane. (g) - (i) 2D planar cut of (a) - (c) at respective ϕ-planes.

Table 4 Summary of results for the 30 GHz $4\lambda_0 \times 4\lambda_0$ TEM HBA dual beam radiation example.

	Beam	Directivity (dB)	3 dB Beamwidth	
			ϕ-plane (°)	θ-plane (°)
Figure 5(a)	I	15.5	20.1	21.5
	II	15.9	21.6	21.4
Figure 5(b)	I	16.4	21.7	18.5
	II	16.2	19.9	21.6
Figure 5(c)	I	16.5	20.2	21.6
	II	16.4	18.9	21.6

We now demonstrate other possibilities with multiple beam generation. Whereas the previous example shows radiation with two beams of equal intensity, the Huygens box allows one to control the intensity of each radiated beam by simply incorporating the required intensity levels into E_{i0} when calculating the excitation currents for constituent Huygens sources. Following this procedure, one may generate any number of plane waves propagating in many directions with arbitrary amplitudes and couple such waves to directive radiation. The azimuthal direction of the cavity wave maps directly to the azimuthal direction of the radiated beam through (14), while the elevation angle is related to the refractive index of the enclosed region through (6) or (15). As an example, in Figure 6(a) and (b) we synthesize a pair of beams in directions (ϕ,θ) of $(210°, 45°)$ and $(120°, 45°)$, and a power intensity ratio of 2:1. To achieve this, we set $(E_{10}, E_{20}) = (\sqrt{2}, 1)$ in (2) and calculate the necessary excitations currents using (3). From the 2D plots of Figure 6(a) and (b), we observe a corresponding 3.2 dB difference in the intensity levels for the two beams. This conforms reasonably to the expected 3 dB difference expected for such intensity levels. We summarize the results in Table 5 .

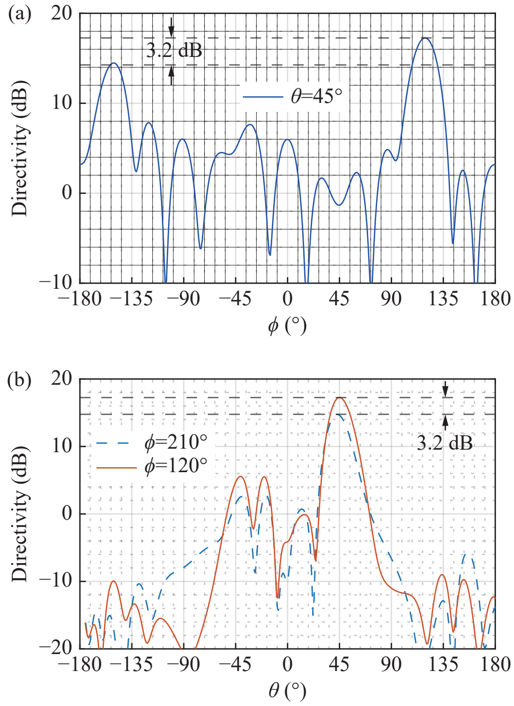

Figure 6 A demonstration of dual beam generation with arbitrary beam strengths, with beams radiated towards $(\varphi,\theta)=(210°,45°)$ and $(120°,45°)$ with beam intensity ratio of 1:2 plotted at (a) $\theta=45°$-plane and at (b) $\varphi=210°,120°$-planes, respectively.

Furthermore, Figure 7(a) shows multi-beam generation consisting of eight antenna beams spaced 45° apart.

Table 5 Dual beam generation with beam intensity ratio of 2:1.

$\theta(°)$	$\phi(°)$	Directivity (dB)	3 dB Beamwidth	
			ϕ-plane (°)	θ-plane (°)
45°	210°	14.1	19.8	20.9
	120°	17.3	19.1	21.8

This pattern emanates from a superposition of eight plane waves with respective wavevectors defined by $\boldsymbol{k_n}=(k\cos\varphi_n, k\sin\varphi_n, 0)$ where $\varphi_n=\varphi_0+(n-1)\Delta\varphi$, $\varphi_0=0°$, $n=1,2,\ldots,8$ and $\Delta\varphi=45°$. Figure 7(b),(c) show the antenna pattern of a 40°-wide sector beam. These results demonstrate the versatility of the proposed antenna to adapt to many useful applications including but not limited to long distance communication, imaging, radar systems, autonomous vehicular technology and the Internet of Things.

3. Experiment Results

For fabrication simplicity, we perform an experimental demonstration at a microwave frequency of 7.5 GHz. In this experimental demonstration, we implement the simplified single filament Huygens source wherein we drive necessary excitation currents through a conductive rod backed by a metal plate. The enclosing cavity, bottom and perforated top plates are made from 2 mm-thick aluminium plates. We build the enclosed sub-unity refractive index metamaterial region by positioning copper rods in a rectangular lattice formation (as shown in Figure 2(a)) into a low-density foam that fills the cavity. The low-density foam behaves similar to air at this frequency and serves to provide mechanical support for equispaced rods that form the artificial dielectric medium. The rods extend from the bottom plate to the perforated top plate. Figure 8(a) shows the fabricated $4\lambda_0\times4\lambda_0$ Huygens box antenna with the perforated top uncovered to show the otherwise enclosed sub-unity index

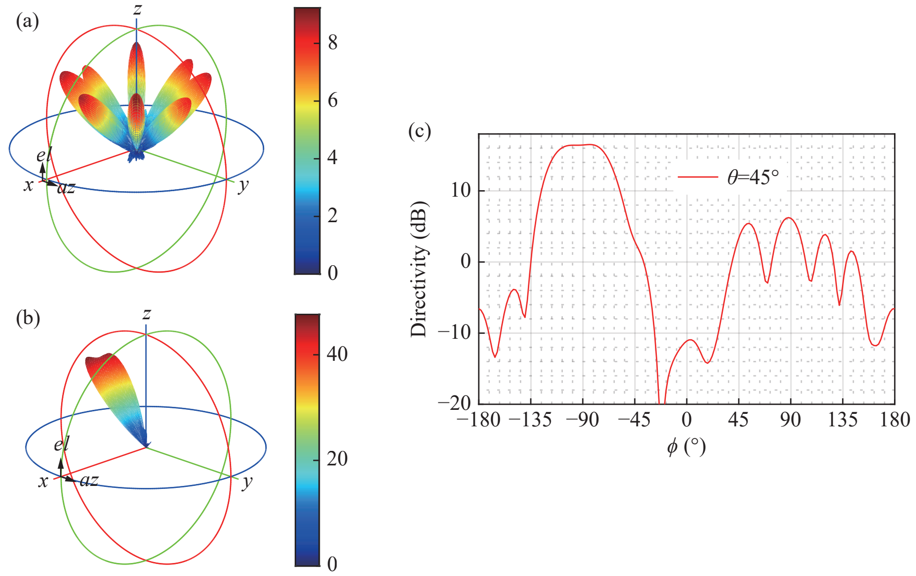

Figure 7 Some more possibilities of multiple beam generation. (a) Octal-beam radiation with beams spaced at 45° apart. (b) A 45°-wide sector beam radiation. (c) 2D planar cut of (d) at θ = 45° plane.

metamaterial, while Figure 8(b) shows the antenna in the test chamber.

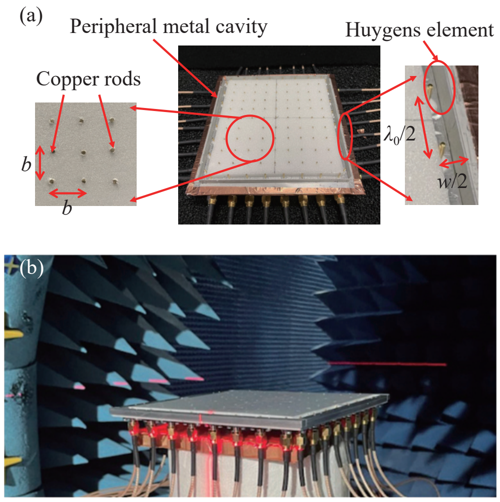

Figure 8 The fabricated all-metal antenna and measurement setup. (a) The TEM Huygens box antenna with the perforated top plate uncovered. (b) The antenna in the Satimo test chamber.

To achieve continuous steering of the radiation, an electronically controlled phase-shift network with amplitude and phase modulation capabilities would be required. While amplitude and phase modulations offer complete flexibility for multiple beam generation, only phase modulation is required for single beam generation. For simplicity in this paper, we design power dividers with custom-designed phase shifts to achieve fixed beam radiation to specific directions with the Huygens box antennas. We fabricate three excitation networks for $\varphi_0 = 0^\circ$, $\varphi_0 = 30^\circ$ and $\varphi_0 = 45^\circ$. Exploiting the symmetry of the Huygens box, we then use port reconnections and feed network rotations to achieve radiation to $\varphi_0 = m_p 30^\circ$ where $m_p = 0$ to 11 and $\varphi_0 = n_p 45^\circ$ where $n_p = 0$ to 7, thus allowing us to demonstrate beamforming with 360° coverage in the azimuthal direction in steps of 30° and in steps of 45°.

In the following, we label Port 0 (P0) as the input and Ports 1-32 (P1 – P32) as the 32 outputs of the feed network. The measured return loss of the feed network designed to synthesize a propagating plane wave at $\varphi = 0^\circ$ is −12 dB (similar loss levels are observed for the other cases). The extracted simulated and measured power at the output ports $P1$ to $P32$ are tabulated in Error! Reference source not found.. To satisfy the law of conservation of power

$$\mathrm{P}_0 = \mathrm{P}_0\left[|\mathrm{S}_{00}|^2 + \sum_{\mathrm{n}=1}^{32}|\mathrm{S}_{\mathrm{n}0}|^2\right] + \mathrm{PL} \tag{16}$$

where PL represents other losses from the feed network comprising the substrate and metal losses. The term $\sum_{\mathrm{n}=1}^{32}|\mathrm{S}_{\mathrm{n}0}|^2$ represents the forward transmission efficiency of the feed network. Using the extracted values in Error! Reference source not found., the feed network fabricated to radiate to $(\varphi,\theta) = (0^\circ, 45^\circ)$, therefore, has a forward transmission efficiency of 71.6%. Accounting for the reflection loss, substrate and metal losses, the proportion of the input power drawn by the Huygens box antenna in an ideal case where the Huygens sources are well-matched to the feed network is, therefore, $P_{in.HBA} = P_0 \times \left[\sum_{\mathrm{n}=1}^{32}|\mathrm{S}_{\mathrm{n}0}|^2\right]$, which is then split into 32 parts to excite the constituent Huygens sources.

We measure the radiation pattern emanating from the Huygens box antenna using a Satimo spherical near-field measurement system. The Satimo system features a circular probe array surrounding a rotating platform on which the antenna being measured is placed. The diameter of the probe array is 90 cm. For our measurement, we placed the antenna in the centre of the circular probe array, hence the radial distance from our antenna to the circular probe array is approximately 45 cm. The stage rotates in steps of 3° while the probes array remains stationary. For improved resolution, slight adjustments to the position of the circular probe array create oversampling, ensuring efficient 3D radiation pattern characterization with high spatial resolution. An image of the fabricated antenna under test is shown in Figure 8(b). We show in Figure 9(a)-(d) the respective radiation patterns measured when the antenna is excited to radiate to directions $(\phi,\theta) = (0^\circ, 45^\circ)$, $(30^\circ, 45^\circ)$, $(45^\circ, 45^\circ)$ and $(60^\circ, 45^\circ)$. Clearly, in each case a highly-directive main beam is achieved radiating to the prescribed directions. We compare the measured radiation patterns to the simulated patterns of a comparable HBA designed for operation at 7.5G Hz in Figure 10. Figure 10(a) - (d) plot a 2D planar cut of the measured radiation patterns along the $\theta = 45^\circ$ plane for generated pencil beams towards azimuth directions, $\phi = 0^\circ$, $\phi = 30^\circ$, $\phi = 45^\circ$, and $\phi = 60^\circ$, respectively, while Figure 10 (e) - (h) plot a 2D planar cut of the measured radiation patterns along the respective ϕ planes for generated pencil beams towards azimuth directions, $\phi = 0^\circ$, $\phi = 30^\circ$, $\phi = 45^\circ$, and $\phi = 60^\circ$, respectively. The measured directivity at $\phi = 0^\circ$ is 17 dB, with a sidelobe level well below 10 dB along the $\phi = 45^\circ$ cut. We notice slightly lower directivities for the oblique cases (i.e. $\phi \neq 0^\circ$), averaging about 16.5 dB, with slightly higher sidelobe levels of about 5 dB. This arises from the imbalances in the amplitudes and phases from the feed network, especially for the oblique cases. It is also possible that the metamaterial medium has a refractive index that slightly differs from the intended value of sin 45°. These can lead to the excitation of unwanted modes in the cavity (we performed a sensitivity analysis in Section IV-2). We observe that the unwanted modes, which are more pronounced in the oblique azimuth angles, lead to spurious radiation culminating in slightly lower directivities and higher sidelobes. However, the level is contained to a reasonable extent and has not degraded the radiation to an unacceptable level for an experimental demonstration. A suitable electronic beamformer with stringent error margins will alleviate this problem.

Essentially, the fabrication process of the metasurface-enabled cavity, the sub-unity refractive index medium and

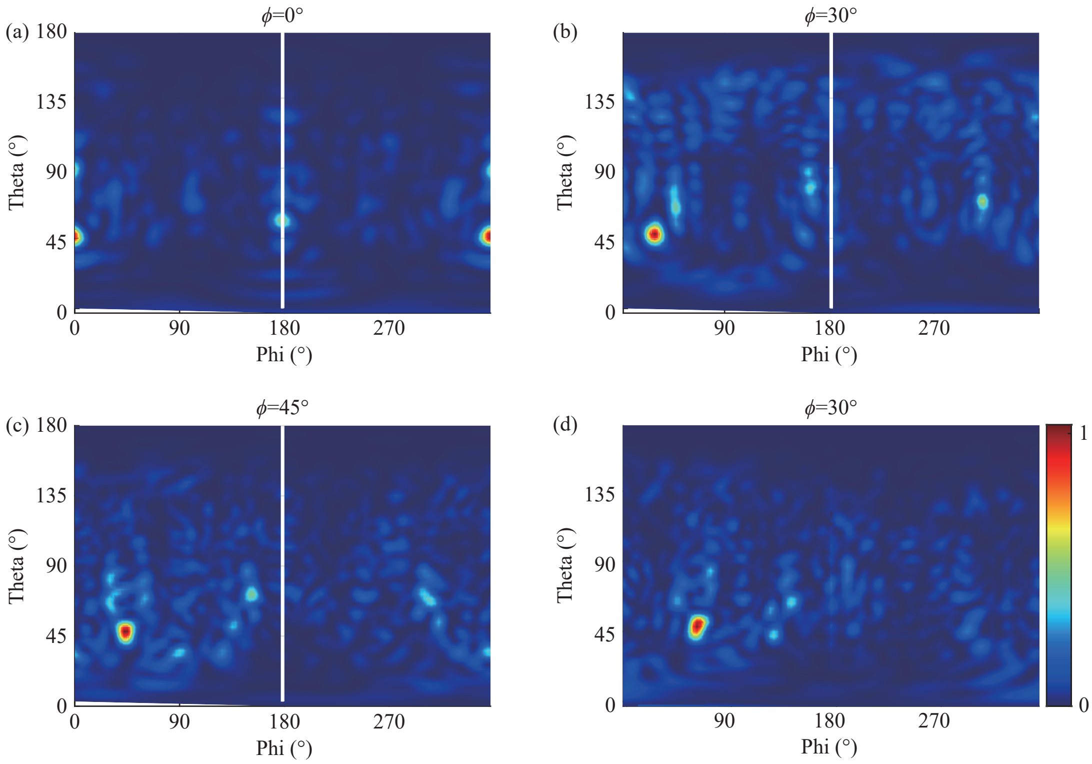

Figure 9 Measured 3D radiation patterns with the HBA excited to radiate to (ϕ,θ) = (a) $(0°,45°)$, (b) $(30°,45°)$, (c) $(45°,45°)$, (d) $(60°,45°)$.

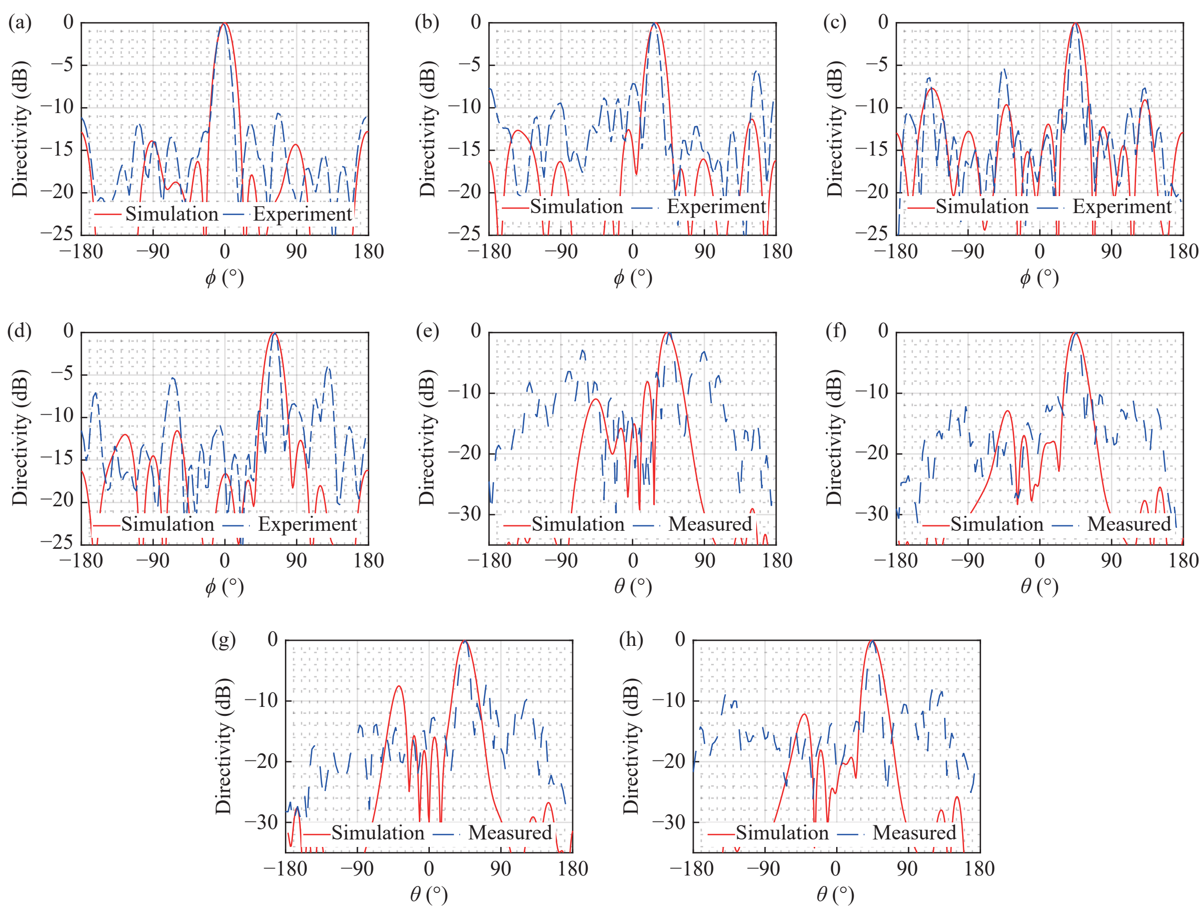

Figure 10 A comparison of the simulated and measured radiation patterns. (a) – (d) show 2D planar cuts along the $\theta = 45°$-plane. (e) – (h) show 2D planar cuts along the $\phi = 0°, 30°, 45°$ and $60°$ planes.

the feed network employ proven microwave techniques. While this is a widely recognised advantage of the conventional microstrip patch phased array, the Huygens box antenna presented also reduces the complexity and component cost, especially in large arrays, through the achieved dramatic reduction in the number of fed elements.

IV. Discussions

In this study, we aimed to provide an alternative to phased arrays for continuous and highly directive beamforming using the HBA. We have shown, through simulations and experiments, directive beamforming with significant reductions in the number of active elements required. This section will discuss the implications of these findings and some important considerations.

1. Inter-element mutual coupling

As our antenna features many closely spaced Huygens elements, we begin with a discussion on the inter-element mutual coupling. A monopole antenna exhibits an omnidirectional radiation pattern in the plane perpendicular to the monopole. As anticipated, when two monopoles are placed in proximity, there is a high level of mutual coupling. Like all Huygens sources, the metal-backed single filament Huygens element employed in this research possesses directional propagation or radiation in both the near-field and far-field. Exploiting this distinctive near-field directionality, we can reduce coupling between adjacent Huygens sources without the need for an external decoupling network. The inherent mutual coupling suppression of the adopted Huygens sources is illustrated in the sample simulation depicted in Figure 11. Figure 11 presents an HFSS model for a pair of monopoles in free space (Figure 11(a)), a pair of monopoles in the Parallel Plate Waveguide (PPW) environment (Figure 11(b)), and a pair of Huygens elements (Figure 11(c)) with elemental separation, s. Simulated mutual coupling ($S21$) is plotted for cases (a) - (c) over a range of separations from $0.15\lambda_o$ to λ_o at intervals of $0.05\lambda_o$ in Figure 11(d). It is evident that mutual coupling is significantly suppressed in the case of Huygens sources compared to monopoles in free space and in the PPW environment. As the inter-element separation s increases, mutual coupling suppression is observed to increase. Importantly, for an element separation of $0.5\lambda_o$ adopted in this research, mutual coupling is suppressed to below −26 dB (over 13 dB when compared to a conventional monopole pair). While the discussion in this section is focused on mutual coupling suppression using the metal-backed active Huygens source, we have delved into the use of directional dipoles – Huygens and Janus sources – for near-field mutual coupling suppression in greater detail in [48].

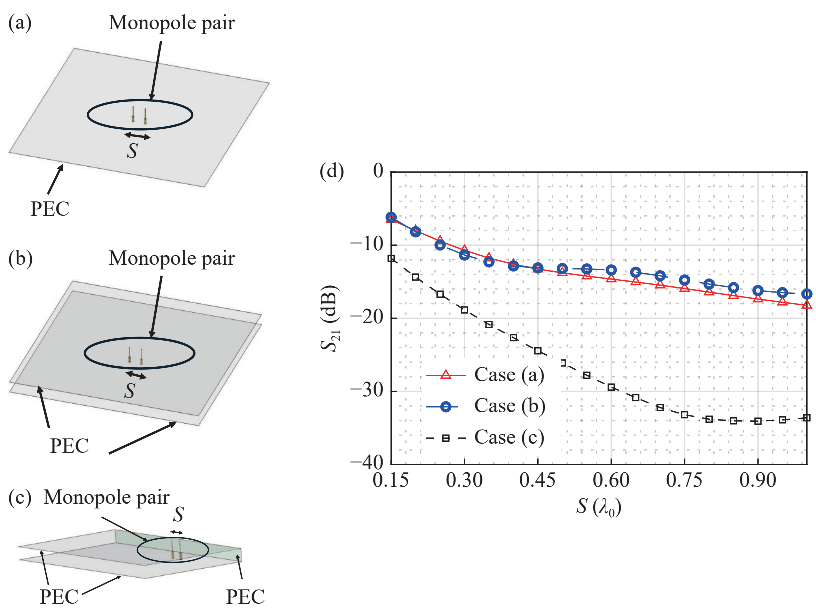

Figure 11 Mutual coupling suppression capability of the Huygens source. (a) A pair of monopoles on a ground plane. (b) A pair of monopoles in a PPW environment. (c) A pair of the PEC-backed single filament Huygens sources. (d) A plot of the mutual coupling as a function of element separation, s, for (a) - (c).

2. Sensitivity analysis

We now investigate, in simulation, the robustness of the Huygens box antenna when the current excitation weightings, as well as the cavity refractive index, slightly differ from the ideal cases. This is important with a view to physical application, as a number of factors including fabrication tolerances, component tolerances and misalignment in rod placement may introduce slight errors into such values.

First, we consider the effect of variations in the refractive index of the sub-unity medium. We simulate the Huygens box antenna and excite the constituent Huygens elements to radiate to direction $(\phi, \theta) = (0°, 45°)$. The radiation criterion stipulates that the cavity has a refractive index $n = \sin 45° = 0.7071$, with the Huygens elements excited to synthesize a plane wave propagating at $\phi = 0°$. To investigate the effect of deviations in the cavity's index on the radiation characteristics, we introduce some errors into the index, n, while keeping the complex excitations to synthesize the propagating plane wave at $\phi = 0°$. Figure 12(a)-(b) plot the directivity for a few iterations of the refractive index around the required $n = 0.7071$. We observe that in terms of the beam pointing directions and the beamwidths, the antenna performance shows great agreement for $n = 0.6928, 0.7071$ and 0.7211. However, as the index differs further, the radiation deteriorates as evidenced by the slight reduction in directivity and higher sidelobe levels observed when $n = 0.6708$ and 0.7416.

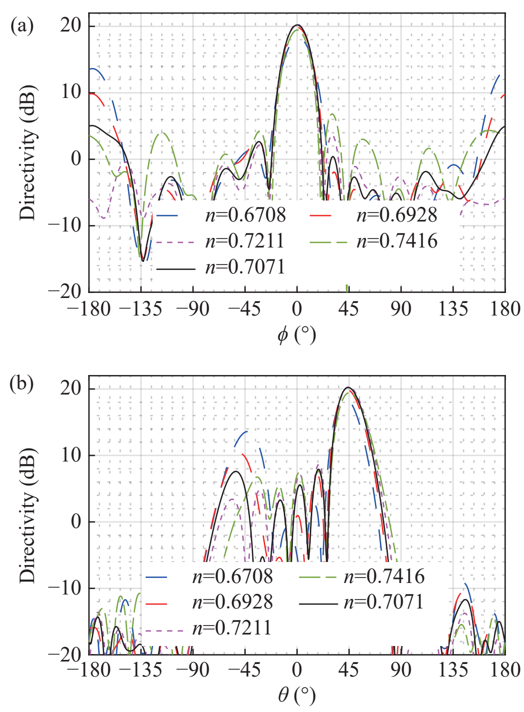

Figure 12 Effect of cavity's refractive index on the radiation characteristic of the Huygens box antenna. The refractive indices were assigned in HFSS using material property ε_r, where $n = \sqrt{\varepsilon_r}$. (a) and (b) are phi-plane and theta plane cuts respectively.

Next, we investigate the effect of deviations in the complex excitation weightings on the radiation performance of the Huygens box antenna. These deviations manifest as amplitude and phase imbalances in the associated feed network. We consider the single-beam radiation case. We hence introduce random imbalances into the equiamplitude current excitations. These imbalances were modelled by a vectorial addition of a randomly phased white Gaussian component with a mean amplitude specified as a percentage of the current amplitude. In order to closely mimic the experimental setup, the simulation implements the $n = 0.7071$ rodded dielectric medium with rod separations calculated by (9). We observe that imbalances of up to 30% do not impact the synthesized wave travel direction, although spurious modes are introduced in unwanted directions. However, as shown in Figure 13(a) - (h), the strength of the spurious modes is generally not strong enough to significantly degrade the radiated wave beyond slightly reduced directivity and higher back lobes.

3. Element reduction ratio

Here, we illustrate the attractiveness of the HBA by demonstrating its dramatic reduction in the number of active radiating elements in comparison to a phased array antenna. For simplicity, we consider a square $m\lambda_0 \times m\lambda_0$ aperture. For a phased array with a center-to-center element spacing of $\lambda_0/2$, the aperture ***area*** will be placed with equispaced phased elements, each occupying an area of $(\lambda_0/2)^2$. Hence the total number of phased elements is

$$N_{PA} = \frac{Area}{(\lambda_0/2)^2} = \left[\frac{m\lambda_0}{(\lambda_0/2)}\right]^2 = 4m^2. \tag{17}$$

On the other hand, for the Huygens box antenna, the phased elements will be equispaced with a separation of $\lambda_0/2$ along the ***perimeter*** of the aperture. Hence the number of phase elements is

$$N_{HBA} = \frac{Perimeter}{(\lambda_0/2)} = \left[\frac{4m\lambda_0}{(\lambda_0/2)}\right] = 8m. \tag{18}$$

We note, from (17) and (18), that N_{PA} is proportional to m^2 while N_{HBA} is proportional to m. Hence for electrically large (i.e. highly directive) antennas, for which $m \gg 1$, it follows that $N_{HBA} \ll N_{PA}$. For the square aperture size of $m\lambda_0 \times m\lambda_0 (m \gg 1)$, employing the Huygens box concept will yield an element reduction ratio of

$$\text{Reduction ratio} = \frac{N_{PA}}{N_{HBA}} = m/2. \tag{19}$$

Figure 14 shows the achievable reduction ratios for some aperture sizes. For instance, forming a $32\lambda_0 \times 32\lambda_0$ beamforming aperture using a Huygens box antenna as opposed to a phased array results in a 16-fold reduction (i.e 4,096 to 256) of phased elements. Similar reduction ratios can be obtained for apertures of arbitrary shapes. This makes the Huygens box antenna very attractive for electrically large and highly directive arrays. A further reduction in the number of elements is envisaged by incorporation phase wavefront engineering into the Huygens box concept [49]–[52].

4. Element separation beyond $\lambda_0/2$

We now discuss the possibility of element separation greater than half free space wavelength for the TEM HBA. The element separation affects the extent of a discrepancy region [32] around the Huygens elements that influences the cavity wave. The discrepancy region refers to an area surrounding the Huygens element within which the strong near-fields of the sources may make the overall waveform deviate from the stipulated cavity wave. This discrepancy

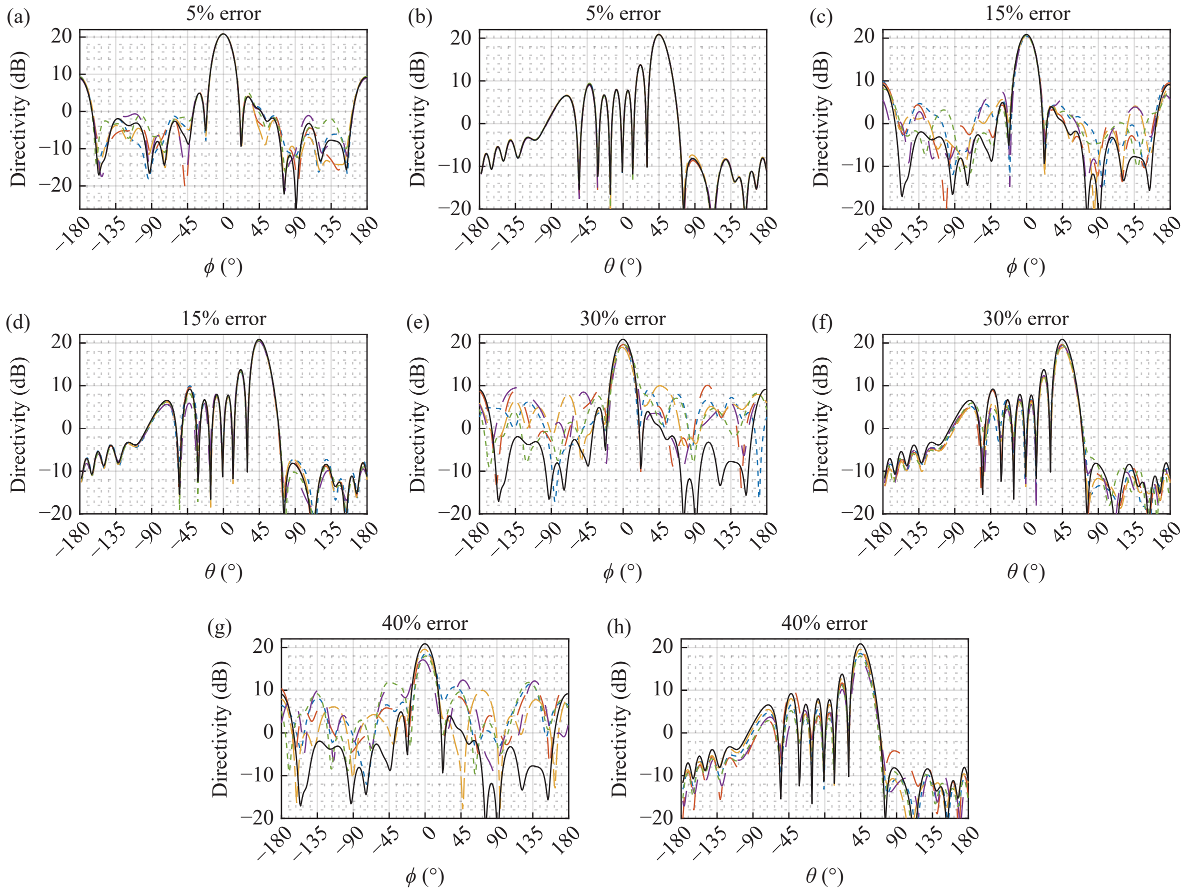

Figure 13 Introducing variations into the excitations to study the effect of amplitude and phase imbalances on the radiated wave. (a)-(b) plot the 2D patterns along $\theta = 45°$ and $\phi = 0°$ planes respectively when excitation currents are varied by 5%. Similarly, (c)-(d) plot the 2D patterns when excitation currents are varied by 15%, (e)-(f) plot the 2D patterns when excitation currents are varied by 30%, and (g)-(h) plot the 2D patterns when excitation currents are varied by 40%. In all cases, the ideal scenario is plotted in black lines for comparison.

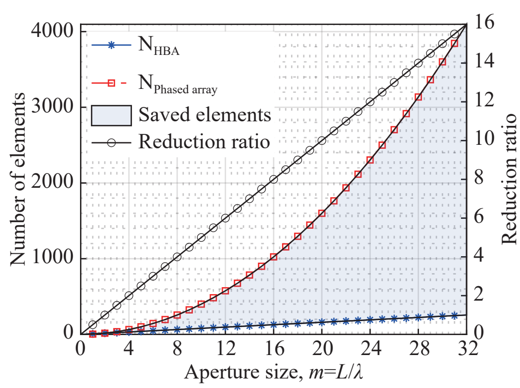

Figure 14 Fed element reduction ratio of the Huygens box compared to a phased array for a square $m\lambda_0 \times m\lambda_0$ aperture.

region δ can be estimated using $\delta = w/2 + s/(\pi\sqrt{(1-(2s/\lambda)^2)})$, where $w/2$ is the filament-to-cavity-wall separation, s is the Huygens sources separation, and $\lambda = \lambda_0/n$. Essentially, the active elements of the Huygens box need to be separated less than or equal to $\lambda_0/2n$ in order to satisfy the Nyquist sampling condition: a sparser separation leads to aliasing in the spatial frequency (k_t-) space, and result in the generation of wave components in spurious directions. An estimate of the discrepancy region is plotted for different cavity media in Figure 15(a). We see from Figure 15(a) that while an element spacing of $0.4\lambda_0$ limits δ to about $0.2\lambda_0$ in the sub-unity index ($\mu_r = 1, \varepsilon_r = 0.5$) metamaterial, a dense material ($\mu_r = 1, \varepsilon_r = 2.2$) requires a finer discretization level ($< 0.35\lambda_0$) to limit δ to a reasonable level. Since the TEM antenna presented here encloses a region of sub-unity refractive index, it then follows that the Huygens elements may be spaced even farther, leading to a further reduction in the number of fed elements. To radiate to the elevation direction $\theta = 45°$, the enclosed region needs to have an index $n = 0.7071$, which means the maximum separation is $\lambda_0/2n = 0.7071\lambda_0$. We therefore consider a case of elements separated at a distance $s = 0.67\lambda_0$ from one another. The simulated results are shown in Figure 15(b),(c). It is observed that in terms of the beam pointing direction, directivity and beamwidths, the antenna achieves similar radiation performance as a reference phased array, with a further reduction in the number of elements required at the expense of slightly higher sidelobe levels. Specifically, for a $4\lambda_0 \times 4\lambda_0$ aperture, the number of elements required reduces from 32 (for $s = 0.5\lambda_0$) to 24 (for $s = 0.67\lambda_0$). Regardless of the choice of s, a substantial reduction has been achieved compared to a conventional phased array of the same aperture size which would require 64 elements.

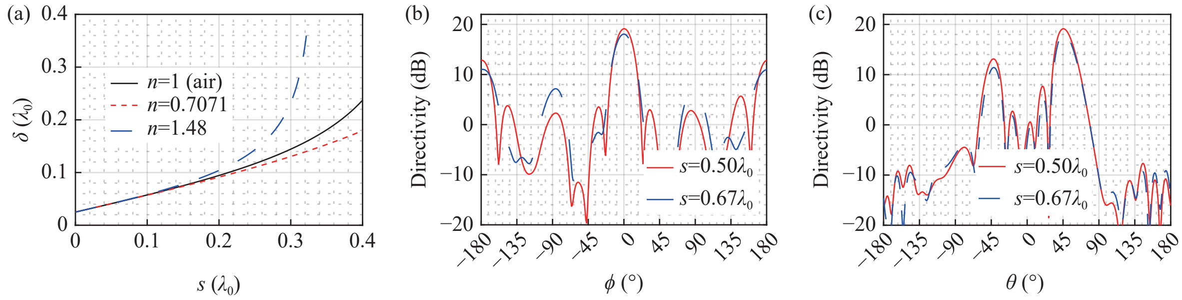

Figure 15 Element separation beyond half free space wavelength. (a) An estimate of the discrepancy region for different media. (b) A planar cut of the radiation pattern along the $\phi = 0°$ plane when $s = 0.5\lambda_0$ and $0.67\lambda_0$. (c) A planar cut of the radiation pattern along the $\theta = 45°$ plane when $s = 0.5\lambda_0$ and $0.67\lambda_0$.

5. Aperture efficiency

We compare the directivity of the Huygens box antenna to a conventional patched antenna array with the same aperture area. For conventional phased arrays, the effective aperture scales with a factor of cosθ, where θ is the elevation angle from broadside direction. The directivity of such an array is given by $10\log_{10}\frac{4\pi}{\lambda^2}A\cos\theta$. The Huygens box antenna features an aperture area $A = 3.8\lambda_0 \times 3.8\lambda_0$ (the extent of the perforations on the top plate). We hence proceed to simulate a patch antenna array with the same aperture area and the same frequency of 30 GHz. Figure 16(a) shows a unit cell of the antenna array. The antenna is excited as a current source across the $\lambda_0/5 \times \lambda_0/5$ metallic patch at the center of the cell. The cell's lateral size is $0.475\lambda_0 \times 0.475\lambda_0$; we simulate an 8×8 repetition of the unit cell along the x- and y-directions using the HFSS array setup. This yields a 64-element $3.8\lambda_0 \times 3.8\lambda_0$ microstrip patch array, whose radiation characteristics can now be compared with the Huygens box. Figure 16(b) plots the directivity values achieved by the Huygens box antenna and the patch array antenna over $0° \leq \phi \leq 90°$. Similar comparison can be deduced for other azimuth angles using the symmetric geometry of the antenna. We observe that the Huygens box antenna achieves a directivity very close to that of the microstrip patch array, which means that the relative aperture efficiency is mostly over 80%. The achievement of such a high aperture efficiency with a dramatic reduction in the number of sources makes the Huygens box antenna very attractive for large-aperture antenna beam-steering applications.

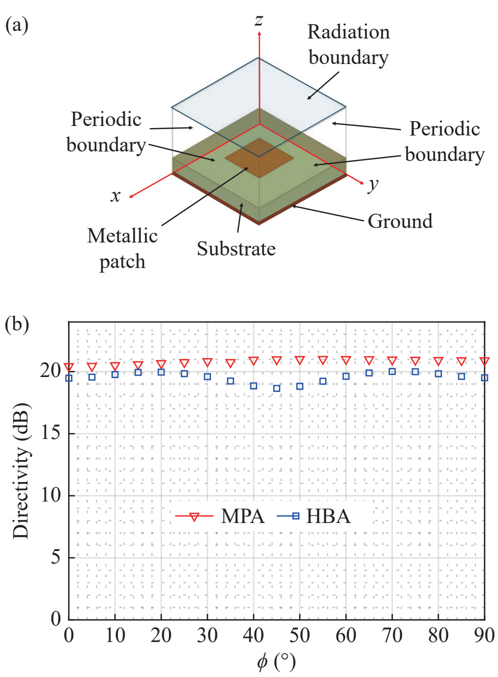

Figure 16 Relative aperture efficiency. (a) A unit cell of the comparative microstrip patch array (MPA). (b) Simulated directivity over $0° \leq \phi \leq 90°$ for a $4\lambda_0 \times 4\lambda_0$ aperture microstrip patch array (MPA) and the TEM Huygens box antenna (HBA). Directivities at other angles can be inferred by geometry.

6. Frequency-dependent elevation beam steering

The enabling sub-unity refractive index cavity of the Huygens box antenna is implemented with a 2D array of metallic rods at separation, b, from one another as discussed in Section II-2. Hence, one can exploit the dispersive characteristics of the metamaterial cavity in the TEM HBA to achieve elevation beam steering. When the frequency varies, the refractive index of the cavity undergoes changes while maintaining a constant rod separation, as illustrated in Figure 17(a) with b = 4.2 mm. Given that the elevation angle θ is related to the refractive index through $\theta = \sin^{-1}n$, one can recalibrate and apply the appropriate excitation to the Huygens sources to steer the elevation angle according to the updated cavity index. Figure 17(b) shows the change in the elevation angle θ as a function of frequency for a fixed rod separation of b = 4.2 mm. From the figure, we see that the elevation angle can be steered from 30° to 60° by choosing the correct operation frequency. This shows the versatility of the TEM HBA for applications over a range of frequencies, enhancing flexibility in various applications.

7. Bandwidth analysis

The Huygens box that forms the foundation for this antenna itself has a reasonable bandwidth of about 10% [32]. This means that a specified wave can be regenerated over this bandwidth provided that the cavity's index does not change with frequency. However, the enabling metamaterial region that we have used to facilitate radiation to a tilted elevation angle in this paper is dispersive, and its index

Table 6 Excitation weightings Excitation currents required to generate a single pencil beam to direction $(\phi,\theta) = (0°,45°)$.

Port	Calculated		Extracted		Measured	
	Mag (W)	Phase (deg)	Mag (W)	Phase (deg)	Mag (W)	Phase (deg)
P1	0.031	59.12	0.026	60.32	0.022	59.51
P2	0.031	59.12	0.027	59.79	0.020	62.06
P3	0.031	59.12	0.027	59.39	0.022	60.76
P4	0.031	59.12	0.026	59.70	0.019	61.82
P5	0.031	59.12	0.026	59.94	0.019	62.07
P6	0.031	59.12	0.027	59.37	0.022	60.82
P7	0.031	59.12	0.027	59.40	0.023	59.09
P8	0.031	59.12	0.027	60.20	0.020	64.17
P9	0.031	175.48	0.027	−0.01	0.033	157.37
P10	0.031	48.20	0.026	51.49	0.028	55.31
P11	0.031	100.92	0.027	100.61	0.021	111.71
P12	0.031	153.64	0.027	−24.67	0.023	140.66
P13	0.031	26.36	0.027	27.30	0.028	21.83
P14	0.031	79.08	0.026	78.44	0.020	82.98
P15	0.031	131.80	0.027	−51.23	0.015	114.41
P16	0.031	4.52	0.027	2.59	0.041	−4.16
P17	0.031	120.88	0.026	117.96	0.017	110.60
P18	0.031	120.88	0.026	117.06	0.020	113.20
P19	0.031	120.88	0.027	116.97	0.019	109.45
P20	0.031	120.88	0.027	117.60	0.016	106.93
P21	0.031	120.88	0.026	117.60	0.017	107.83
P22	0.031	120.88	0.026	116.95	0.017	110.82
P23	0.031	120.88	0.026	117.21	0.017	112.35
P24	0.031	120.88	0.026	118.38	0.016	111.80
P25	0.031	4.52	0.027	2.95	0.037	158.74
P26	0.031	131.80	0.027	−50.64	0.014	110.60
P27	0.031	79.08	0.026	78.60	0.015	77.03
P28	0.031	26.36	0.027	27.46	0.039	26.50
P29	0.031	153.64	0.027	−25.92	0.022	130.17
P30	0.031	100.92	0.026	99.34	0.017	105.49
P31	0.031	48.20	0.026	50.31	0.025	60.97
P32	0.031	175.48	0.027	−1.03	0.033	157.32

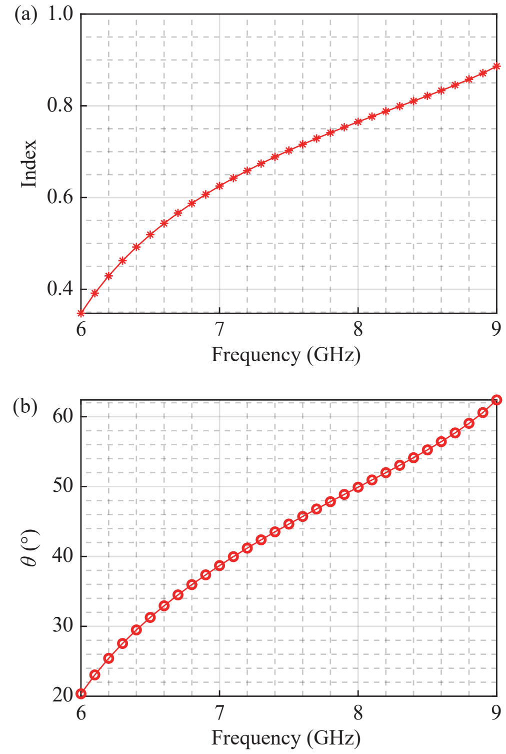

Figure 17 TEM HBA frequency-dependent elevation beam steering. (a) A plot of the refractive index with respect to frequency for a fixed rod separation, $b = 4.2$ mm. (b) Elevation beam steering with frequency change.

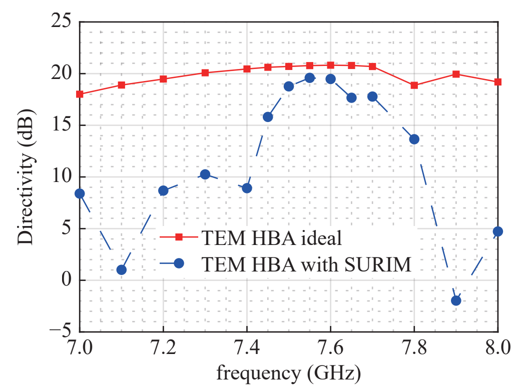

Figure 18 Bandwidth evaluation. The TEM HBA Ideal models a non-changing cavity index, while the TEM HBA with SURIM models the sub-unity index cavity with the rods array.

varies with frequency. If one can somehow change the cavity's index as frequency changes, a similar bandwidth to the base Huygens cavity can be achieved. Figure 18 shows the directivity as a function of frequency for the "Ideal TEM HBA" whereby the refractive index does not change with frequency and for our current model, the "TEM HBA with SURIM" (where SURIM denotes Sub-Unity Refractive Index Metamaterial), that achieves the required sub-unity index with the rodded artificial dielectric medium. Results show that while the dispersive nature of the metamaterial limits the 3 dB directivity bandwidth of our antenna to 3.3%, the simulated 3 dB directivity bandwidth of 13.3% for the ideal case reiterates the fact that a decent bandwidth can be achieved if real-time index change can be achieved.

V. Conclusion

In this paper, we explore the generation of propagating electromagnetic waves in a Huygens box and its application to directive beamforming. We show the generation of single beams, multiple beams, sector beams and beam steering. The fabrication procedure for this metasurface-enabled Huygens box antenna is relatively straightforward as it employs conventional array technology which is mature. The enabling metamaterial region is also easily formed by arranging metallic rods at appropriate separation within the cavity. We show that the radiated waves emanating from the HBA have a comparable directivity to a microstrip patch array having a similar aperture size, while the number of phased elements is dependent on the aperture perimeter instead of the aperture area. This results in a $m/2$-fold reduction of phased elements for a square $m\lambda_0 \times m\lambda_0$ aperture, leading to dramatic (beyond 10-fold) reductions for electrically large antennas. The strong reduction in the phased elements will very much simplify the construction, lessen the weight, and lower the cost for electrically large, highly directive and high-frequency antennas, making it an attractive candidate for highly-directive imaging and communication applications in the mm-wave regime.

Acknowledgement

This work was supported by the Research Grants Council of Hong Kong under Projects CityU 21211619, AoE/E-101/23-N and 7006088.

References

[1] L. C. Godara, "Applications of antenna arrays to mobile communications. I. Performance improvement, feasibility, and system considerations," *Proceedings of the IEEE*, vol. 85, no. 7, pp. 1031–1060, 1997.

[2] F. Ahmed, K. Singh, and K. P. Esselle, "State-of-the-art passive beam-steering antenna technologies: Challenges and capabilities," *IEEE Access*, vol. 11, pp. 69101–69116, 2023.

[3] I. Uchendu and J. R. Kelly, "Survey of beam steering techniques available for millimeter wave applications," *Progress in Electromagnetics Research B*, vol. 68, pp. 35–54, 2016.

[4] M. J. Teng, S. X. Yu, N. Kou, *et al*., "Mechanical beam steering array antenna with tunable height," *IEEE Antennas and Wireless Propagation Letters*, vol. 21, no. 11, pp. 2293–2297, 2022.

[5] C. W. Baek, S. Song, C. Cheon, *et al*., "2-D mechanical beam steering antenna fabricated using MEMS technology," in *2001 IEEE MTT-S International Microwave Sympsoium Digest (Cat. No. 01CH37157)*, Phoenix, AZ, USA, pp. 211–214, 2001.

[6] R. J. Mailloux, *Phased Array Antenna Handbook*, 3rd ed. , Artech House, Norwood, 2017.

[7] L. C. Godara, "Application of antenna arrays to mobile communications. II. Beam-forming and direction-of-arrival considerations," *Proceedings of the IEEE*, vol. 85, no. 8, pp. 1195–1245, 1997.

[8] P. Rocca, G. Oliveri, R. J. Mailloux, *et al*., "Unconventional phased array architectures and design methodologies—A review," *Proceedings of the IEEE*, vol. 104, no. 3, pp. 544–560, 2016.

[9] T. Isernia, M. D'Urso, and O. M. Bucci, "A simple idea for an effective sub-arraying of large planar sources," *IEEE Antennas and Wireless Propagation Letters*, vol. 8, pp. 169–172, 2009.

[10] B. Rupakula, A. H. Aljuhani, and G. M. Rebeiz, "Limited scan-angle phased arrays using randomly grouped subarrays and reduced number of phase shifters," *IEEE Transactions on Antennas and Propagation*, vol. 68, no. 1, pp. 70–80, 2020.

[11] R. L. Haupt, "Thinned arrays using genetic algorithms," *IEEE Transactions on Antennas and Propagation*, vol. 42, no. 7, pp. 993–999, 1994.

[12] V. Murino, A. Trucco, and C. S. Regazzoni, "Synthesis of unequally spaced arrays by simulated annealing," *IEEE Transactions on Signal Processing*, vol. 44, no. 1, pp. 119–122, 1996.

[13] Y. Lo, "A mathematical theory of antenna arrays with randomly spaced elements," *IEEE Transactions on Antennas and Propagation*, vol. 12, no. 3, pp. 257–268, 1964.

[14] X. L. Zhao, C. W. Yuan, L. Liu, *et al*., "All-metal beam steering lens antenna for high power microwave applications," *IEEE Transactions on Antennas and Propagation*, vol. 65, no. 12, pp. 7340–7344, 2017.

[15] C. A. Fernandes, J. R. Costa, E. B. Lima, *et al*., "Review of 20 years of research on microwave and millimeter-wave lenses at "Instituto de Telecomunicaço˜es"," *IEEE Antennas and Propagation Magazine*, vol. 57, no. 1, pp. 249–268, 2015.

[16] T. Kaiser, *Smart Antennas: State of the Art*. Hindawi Publishing Corporation, New York, 2005.

[17] M. Ettorre, R. Sauleau, and L. Le Coq, "Multi-beam multi-layer leaky-wave SIW pillbox antenna for millimeter-wave applications," *IEEE Transactions on Antennas and Propagation*, vol. 59, no. 4, pp. 1093–1100, 2011.

[18] J. Ruiz-Garcia, E. Martini, C. Della Giovampaola, *et al*., "Reflecting Luneburg lenses," *IEEE Transactions on Antennas and Propagation*, vol. 69, no. 7, pp. 3924–3935, 2021.

[19] C. L. Holloway, E. F. Kuester, J. A. Gordon, *et al*., "An overview of the theory and applications of metasurfaces: The two-dimensional equivalents of metamaterials," *IEEE Antennas and Propagation Magazine*, vol. 54, no. 2, pp. 10–35, 2012.

[20] A. B. Li, S. Singh, and D. Sievenpiper, "Metasurfaces and their applications," *Nanophotonics*, vol. 7, no. 6, pp. 989–1011, 2018.

[21] M. Faenzi, G. Minatti, D. González-Ovejero, *et al*., "Metasurface antennas: New models, applications and realizations," *Scientific Reports*, vol. 9, no. 1, article no. 10178, 2019.

[22] J. F. Wang, Y. Li, Z. H. Jiang *et al*., "Metantenna: When metasurface meets antenna again," *IEEE Transactions on Antennas and Propagation*, vol. 68, no. 3, pp. 1332–1347, 2020.

[23] J. H. Zhang, S. Yan, and G. A. E. Vandenbosch, "Composite right/left-handed transmission line metamaterial-inspired small antenna design: Topologies, reconfigurability, and applications," *IEEE Antennas and Propagation Magazine*, vol. 65, no. 1, pp. 71–78, 2023.

[24] A. Krasnok, "Coherently driven and superdirective antennas," *Electronics*, vol. 8, no. 8, article no. 845, 2019.

[25] R. W. Ziolkowski, "Low profile, broadside radiating, electrically small Huygens source antennas," *IEEE Access*, vol. 3, pp. 2644–2651, 2015.

[26] M. M. Nikolic, A. R. Djordjevic, and A. Nehorai, "Microstrip antennas with suppressed radiation in horizontal directions and reduced coupling," *IEEE Transactions on Antennas and Propagation*, vol. 53, no. 11, pp. 3469–3476, 2005.

[27] T. Ming-Chun, X. Shao-Qiu, G. Jian, *et al*., "Composite metamaterial enabled excellent performance of microstrip antenna array," *Chinese Physics B*, vol. 19, no. 7, article no. 074214, 2010.

[28] T. Kokkinos and A. P. Feresidis, "Electrically small superdirective endfire arrays of metamaterial-inspired low-profile monopoles," *IEEE Antennas and Wireless Propagation Letters*, vol. 11, pp. 568–571, 2012.

[29] K. Buell, H. Mosallaei, and K. Sarabandi, "Metamaterial insulator enabled superdirective array," *IEEE Transactions on Antennas and Propagation*, vol. 55, no. 4, pp. 1074–1085, 2007.

[30] K. A. Oyesina, O. Z. Aly, G. G. L. Zhou, *et al*., "Active Huygens' box: Arbitrary synthesis of EM waves in metallic cavities, " in *2019 International Applied Computational Electromagnetics Society Symposium (ACES)*, Miami, FL, USA, pp. 1–2, 2019.

[31] A. M. H. Wong and G. V. Eleftheriades, "Experimental demonstration of the Huygens' box: Arbitrary waveform generation in a metallic cavity," in *2018 IEEE International Symposium on Antennas and Propagation & USNC/URSI National Radio Science Meeting*, Boston, MA, USA, pp. 1893–1894, 2018.

[32] A. M. H. Wong and G. V. Eleftheriades, "Active Huygens' box: Arbitrary electromagnetic wave generation with an electronically controlled metasurface," *IEEE Transactions on Antennas and Propagation*, vol. 69, no. 3, pp. 1455–1468, 2021.

[33] A. H. Dorrah and G. V. Eleftheriades, "Peripherally excited phased array architecture for beam steering with reduced number of active elements," *IEEE Transactions on Antennas and Propagation*, vol. 68, no. 3, pp. 1249–1260, 2020.

[34] A. H. Dorrah and G. V. Eleftheriades, "Experimental demonstra-

tion of peripherally-excited antenna arrays," *Nature Communications*, vol. 12, no. 1, article no. 6109, 2021.
[35] K. A. Oyesina and A. M. H. Wong, "Metasurface-enabled cavity antenna: Beam steering with dramatically reduced fed elements," *IEEE Antennas and Wireless Propagation Letters*, vol. 19, no. 4, pp. 616–620, 2020.
[36] K. A. Oyesina and A. M. H. Wong, "The Huygens' box antenna: Metasurface-based directive antenna beam-steering with dramatically reduced elements," in *2019 IEEE International Symposium on Antennas and Propagation and USNC-URSI Radio Science Meeting*, Atlanta, GA, USA, pp. 443–444, 2019.
[37] K. A. Oyesina and A. M. H. Wong, "Metamaterial-loaded Huygens' box antenna: Highly-directive beam steering with very few phasing elements," in *2020 IEEE Asia-Pacific Microwave Conference (APMC)*, Hong Kong, China, pp. 284–286, 2020.
[38] K. A. Oyesina and A. M. H. Wong, "Experimental demonstration of the metamaterial-based beam-steerable Huygens' box antenna with dramatically reduced phasing elements," in *2022 IEEE International Symposium on Antennas and Propagation and USNC-URSI Radio Science Meeting (AP-S/URSI)*, Denver, CO, USA, pp. 1852–1853, 2022.
[39] S. H. Lee, S. M. Radha, G. Shin, *et al*., "Design of electrically small and thin Huygens source antenna, " in *2018 International Symposium on Antennas and Propagation (ISAP)*, Busan, South Korea, pp. 1–2, 2018.
[40] P. Alitalo, A. O. Karilainen, T. Niemi, *et al*., "A linearly polarized Huygens source formed by two omega particles, " in *Proceedings of the 5th European Conference on Antennas and Propagation (EUCAP)*, Rome, Italy, pp. 2302–2305, 2011.
[41] C. Pfeiffer and A. Grbic, "Metamaterial Huygens' surfaces: Tailoring wave fronts with reflectionless sheets," *Physical Review Letters*, vol. 110, no. 19, article no. 197401, 2013.
[42] A. M. H. Wong and G. V. Eleftheriades, "A simple active Huygens source for studying waveform synthesis with Huygens metasurfaces and antenna arrays," in *2015 IEEE International Symposium on Antennas and Propagation & USNC/URSI National Radio Science Meeting*, Vancouver, Canada, pp. 1092–1093, 2015.
[43] W. E. Kock, "Metallic delay lenses," *Bell System Technical Journal*, vol. 27, no. 1, pp. 58–82, 1948.
[44] J. Brown, "Artificial dielectrics having refractive indices less than unity," *Proceedings of the IEE-Part IV: Institution Monographs*, vol. 100, no. 5, pp. 51–62, 1953.
[45] A. B. Numan and M. S. Sharawi, "Extraction of material parameters for metamaterials using a full-wave simulator [education column]," *IEEE antennas and propagation magazine*, vol. 55, no. 5, pp. 202–211, 2013.
[46] X. D. Chen, T. M. Grzegorczyk, B. I. Wu, *et al*., "Robust method to retrieve the constitutive effective parameters of metamaterials," *Physical Review E*, vol. 70, no. 1, article no. 016608, 2004.
[47] A. Bhattacharyya, "Theory of beam scanning for slot array antenna excited by slow wave," *IEEE Antennas and Propagation Magazine*, vol. 57, no. 2, pp. 96–103, 2015.
[48] B. Xue, K. A. Oyesina, and A. M. H. Wong, "Electromagnetic near-field mutual coupling suppression with active Janus sources," *Communications Physics*, vol. 7, no. 1, article no. 87, 2024.
[49] Y. Y. Yuan, K. Zhang, Q. Wu, *et al*., "Reaching the efficiency limit of arbitrary polarization transformation with non-orthogonal metasurfaces," *Nature Communications*, vol. 15, no. 1, article no. 6682, 2024.
[50] Y. Y. Yuan, Q. Wu, S. N. Burokur, *et al*., "Chirality-assisted phase metasurface for circular polarization preservation and independent hologram imaging in microwave region," *IEEE Transactions on Microwave Theory and Techniques*, vol. 71, no. 8, pp. 3259–3272, 2023.
[51] F. Lan, L. Y. Wang, H. X. Zeng, *et al*., "Real-time programmable metasurface for terahertz multifunctional wave front engineering," *Light: Science & Applications*, vol. 12, no. 1, article no. 191, 2023.
[52] O. A. M. Abdelraouf, Z. Y. Wang, H. L Liu *et al*., "Recent advances in tunable metasurfaces: Materials, design, and applications," *ACS Nano*, vol. 16, no. 9, pp. 13339–13369, 2022.

Kayode Adedotun Oyesina (Member, IEEE) received his Ph.D. in Electrical Engineering from City University of Hong Kong in 2024. He is currently a postdoctoral research fellow at City University of Hong Kong, where his research focuses on applied electromagnetics, including novel directive beamforming, near-field waveguiding, and metasurface technologies. His work explores innovative antenna designs and electromagnetic wave manipulation for potential applications in telecommunications, imaging, autonomous vehicular technology, radar systems, and wireless power transfer.

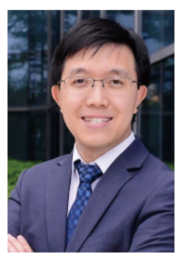

Alex M. H. Wong (Senior Member, IEEE) received the B.A.Sc. degree in engineering science (electrical option) and the M.A.Sc. and Ph.D. degrees in electrical and computer engineering from the University of Toronto, Canada, in 2006, 2009, and 2014, respectively. He then served briefly as a Postdoctoral Fellow with the University of Toronto. Since 2018, he has been an Assistant Professor of Applied Electromagnetics with the Department of Electronic Engineering, City University of Hong Kong, where he is also a member of the State Key Laboratory of Terahertz and Millimeter Waves. He has advanced multiple projects in applied electromagnetics on next-generation RF, infrared, and optical metasurfaces, and super-resolution imaging and radar systems. Particularly, he has made academic contributions to research on wave shaping using Huygens' metasurfaces and far-field imaging based on super-oscillation waves. His current research interests include metasurfaces, metamaterials, and super-resolution systems. His received accolades include an IEEE RWP King Award (for the best annual publication by a young author in the IEEE TRANSACTIONS ON ANTENNAS AND PROPAGATION), the URSI Young Scientist Award, the Raj Mittra Grant, the IEEE Doctoral Research Awards from the AP and MTT societies, and the Canada Graduate Scholarship (doctoral level). He serves as the TPC Vice-Chair for the 2020 Asia–Pacific Microwave Conference. He has taken on various program committee, session chair, technical judge, and reviewer duties for IEEE conferences and journal publications in the AP and MTT societies, as well as relevant venues in applied physics. He is a member of the IEEE Antennas and Propagation Society, Microwave Theory and Techniques Society, and the Photonics Society.